

Dynamic density functional theory for the charging of electric double layer capacitors

Cite as: J. Chem. Phys. **156**, 084101 (2022); <https://doi.org/10.1063/5.0081827>

Submitted: 10 December 2021 • Accepted: 26 January 2022 • Accepted Manuscript Online: 27 January 2022 • Published Online: 22 February 2022

Ke Ma,  Mathijs Janssen,  Cheng Lian, et al.



View Online



Export Citation



CrossMark

ARTICLES YOU MAY BE INTERESTED IN

[The Asakura–Oosawa theory: Entropic forces in physics, biology, and soft matter](#)

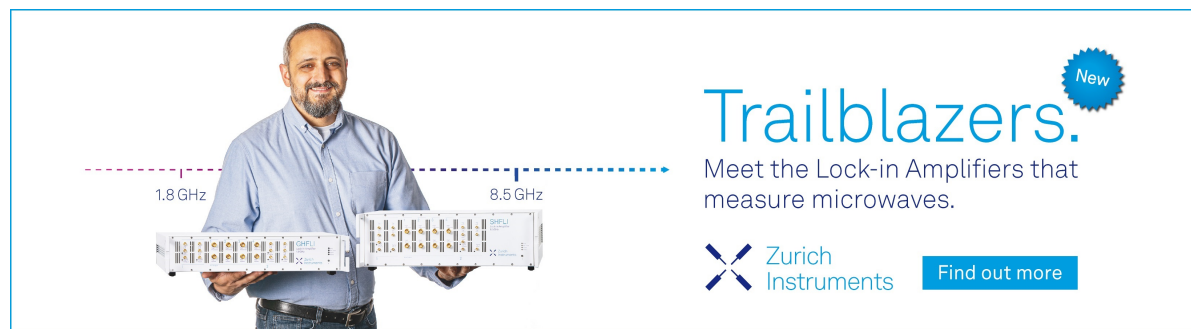
The Journal of Chemical Physics **156**, 080401 (2022); <https://doi.org/10.1063/5.0085965>


[The influence of a Hamiltonian vibration vs a bath vibration on the 2D electronic spectra of a homodimer](#)

The Journal of Chemical Physics **156**, 084103 (2022); <https://doi.org/10.1063/5.0077404>


[On the accuracy and efficiency of different methods to calculate Raman vibrational shifts of parahydrogen clusters](#)

The Journal of Chemical Physics **156**, 084102 (2022); <https://doi.org/10.1063/5.0076403>



Trailblazers. 

Meet the Lock-in Amplifiers that measure microwaves.

 Zurich Instruments [Find out more](#)

Dynamic density functional theory for the charging of electric double layer capacitors

Cite as: J. Chem. Phys. 156, 084101 (2022); doi: 10.1063/5.0081827

Submitted: 10 December 2021 • Accepted: 26 January 2022 •

Published Online: 22 February 2022



View Online



Export Citation



CrossMark

Ke Ma,¹ Mathijs Janssen,²  Cheng Lian,^{3,4,a)}  and René van Roij⁴ 

AFFILIATIONS

¹School of Materials Science and Engineering, Tianjin Key Laboratory for Photoelectric Materials and Devices, National Demonstration Center for Experimental Function Materials Education, Tianjin University of Technology, Tianjin 300384, China

²Mechanics Division, Department of Mathematics, University of Oslo, N-0851 Oslo, Norway

³State Key Laboratory of Chemical Engineering, School of Chemistry and Molecular Engineering, East China University of Science and Technology, Shanghai 200237, China

⁴Center for Extreme Matter and Emergent Phenomena, Institute for Theoretical Physics, Utrecht University, Princetonplein 5, 3584 CC Utrecht, The Netherlands

^{a)} Author to whom correspondence should be addressed: liancheng@ecust.edu.cn

ABSTRACT

We consider the charging of a model capacitor comprised of two planar electrodes and an electrolyte. Upon switching on a voltage difference, electric double layers build up in this setup, which we characterize with a classical dynamic density functional theory (DDFT) that accounts for electrostatic correlations and for molecular excluded volume of finite-sized ions and solvent molecules. Our DDFT predicts the electrode charge $Q(t)$ to form exponentially with two timescales: at early times, the system relaxes on the RC time, namely, $\lambda_D L / [D(2 + \sigma/\lambda_D)]$, with λ_D being the Debye length, L being the electrode separation, σ being the ion diameter, and D being the ionic diffusivity. Contrasting an earlier DDFT study, this early-time response does not depend on the applied potential. At late times, the capacitor relaxes with a relaxation time proportional to the diffusion time L^2/D .

Published under an exclusive license by AIP Publishing. <https://doi.org/10.1063/5.0081827>

I. INTRODUCTION

The dynamics of electrolytes in narrow confinement underlies key functionalities in biology and technology. Examples range from axons firing in the brain¹ and plant-cell signaling by plasmodesmata² to capacitive deionization³ and energy storage by supercapacitors.⁴ In the case of supercapacitors, the dynamics of ions in their porous electrodes can be resolved by molecular simulations^{5–9} and various experimental techniques, including nuclear magnetic resonance spectroscopy,^{10,11} electrochemical quartz crystal microbalance,^{11,12} infrared spectro-electrochemistry,¹¹ and x-ray diffraction.¹³ The structure of electrolytes near solid surfaces has also been studied extensively in the more idealized setting of the surface force apparatus (SFA).^{14,15} In the SFA, two atomically flat surfaces in crossed-cylinder geometry squeeze an electrolyte into nanometric confinement, while the force required to do so is measured. Recently, the SFA has been used to study the response of electrolytes to different time-dependent potential differences

applied to the cylinders.^{16–18} The experiments of Refs. 17 and 18 with curved electrodes were interpreted using flat-electrode models [Fig. 1(a)]. Indeed, much of our theoretical understanding of electrolyte dynamics in narrow confinement derives from flat-electrode models.^{19–38} However, at high electrolyte concentrations, the relation between system parameters and ion dynamics is largely unexplored, even in simple geometries, because of the strong coupling between ionic packing, diffusion, and conduction processes.

In this article, we study the model capacitor of Fig. 1(a) with a dynamic density functional theory (DDFT)³⁹ that accounts for ion–ion correlations, steric packing effects, and dispersion forces, which are all important in concentrated electrolytes.³⁰ We go beyond other DDFT studies on electrolyte relaxation^{30–38} by characterizing not only the time-evolution of the concentration profiles of the ionic species during the electrode charging process but also that of an explicit solvent. Moreover, we elucidate how the relaxation times depend on the Debye length, ionic diameters, electrode separation, and applied potential difference.

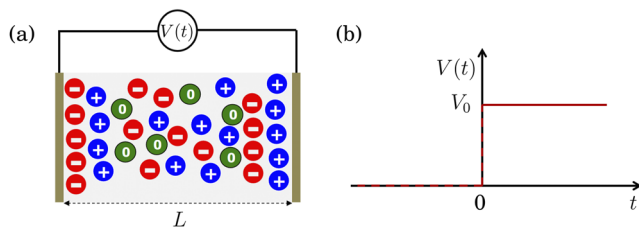


FIG. 1. (a) Model capacitor of two planar electrodes and a three-component electrolyte model of neutral solvent molecules and monovalent cations and anions, all modeled as spheres of diameter σ . (b) The potential difference $V(t)$ between the electrodes switches from 0 V to $V_0 \neq 0$ at time $t = 0$.

II. MODEL

A. Setup

We consider two blocking, flat, and parallel electrodes [Fig. 1(a)] subject to a voltage difference $V(t) = V_0 \Theta(t)$, with $\Theta(t)$ being the Heaviside step function and V_0 being the step size [Fig. 1(b)]. The distance between the two electrodes is L along the x direction; we assume translation invariance in the directions perpendicular to x . The gap between the electrodes is filled with a 1:1 electrolyte of cations, anions, and neutral solvent molecules, labeled $i = \{+, -, 0\}$, respectively, with valencies $z_+ = 1$, $z_- = -1$, and $z_0 = 0$, all modeled as spheres of the same diameter σ . We, thus, have the following boundary conditions:

$$j_i(0, t) = j_i(L, t) = 0, \quad (1a)$$

$$\phi(0, t) - \phi(L, t) = \beta e V(t), \quad (1b)$$

where $j_i(x, t)$ are the particle flux densities, e is the proton charge, and $\beta = 1/(k_B T)$ is the inverse thermal energy, with k_B being Boltzmann's constant and T being the electrolyte temperature. The local electrostatic potential at position $x \in [0, L]$ is given by $(k_B T/e)\phi(x, t)$, with $k_B T/e$ being the thermal voltage and $\phi(x, t)$ being the dimensionless electrostatic potential. As the electrodes are blocking [Eq. (1a)], the number of particles (per unit area) of each species is conserved. This implies that the following global constraints on the time-dependent local concentrations $\rho_i(x, t)$ must be satisfied for all times t :

$$\frac{1}{L} \int_0^L \rho_{\pm}(x, t) dx = \rho_s, \quad \frac{1}{L} \int_0^L \rho_0(x, t) dx = \rho_{\text{sol}}. \quad (2)$$

We refer to the constants ρ_s and ρ_{sol} as the salt and solvent concentrations, where we note, however, that they cannot be identified with the concentrations of a bulk reservoir in osmotic contact with the confined electrolyte. The local concentrations $\rho_i(x, t)$ are coupled to $\phi(x, t)$ by the Poisson equation and to $j_i(x, t)$ by the continuity equation,

$$\partial_x^2 \phi(x, t) = -\frac{\rho_+(x, t) - \rho_-(x, t)}{2\rho_s \lambda_D^2}, \quad (3a)$$

$$\partial_t \rho_i(x, t) = -\partial_x j_i(x, t), \quad (3b)$$

where $\lambda_D = \sqrt{\epsilon_0 \epsilon_r k_B T / 2e^2 \rho_s}$ is the Debye length, with ϵ_0 and ϵ_r being the vacuum and relative permittivity, respectively. For the flux densities $j_i(x, t)$, DDFT asserts that

$$j_i(x, t) = -\beta D \rho_i(x, t) \partial_x \mu_i(x, t), \quad (4a)$$

where D is the diffusion coefficient, presumed equal for all species, and where the chemical potentials μ_i follow from the free energy functional $F[\rho_+, \rho_-, \rho_0]$ as

$$\mu_i(x, t) = \frac{\delta F[\rho_+, \rho_-, \rho_0]}{\delta \rho_i(x, t)}. \quad (4b)$$

To apply Eqs. (1), (3), and (4), $F[\rho_+, \rho_-, \rho_0]$ must be approximated aptly.

A general key weakness of the widely used DDFT approach involves the so-called ‘‘adiabatic approximation’’ that underlies the derivation of Eq. (4); within DDFT, the actual nonequilibrium correlations are replaced by those of a fictitious equilibrium system evaluated at instantaneous nonequilibrium density profiles. To remedy this problem, Power Functional Theory (PFT) was recently proposed as a formally exact alternative to DDFT.⁴⁰ While it would be interesting to use PFT to study the charging of our model setup, unfortunately, no excess power functionals have been developed for ionic systems yet.

B. DDFT formulation

As mentioned, in our setup with planar electrodes, all density profiles depend only on the Cartesian coordinate x . Still, to define $F[\rho_+, \rho_-, \rho_0]$, which accounts for interactions of particles in all three dimensions, it is convenient to use the position vector $\mathbf{r} = (x, y, z)$, where y and z represent the Cartesian coordinates perpendicular to x . We choose $F[\rho_+, \rho_-, \rho_0]$, such that $\mu_i(\mathbf{r}, t)$ from Eq. (4b) is given by

$$\begin{aligned} \mu_i(\mathbf{r}, t) = & k_B T \ln[\rho_i(\mathbf{r}, t) \Lambda_i^3] + k_B T z_i \phi(\mathbf{r}, t) + V^{\text{ext}}(\mathbf{r}) \\ & + \mu_i^{LJ}(\mathbf{r}, t) + \mu_i^{\text{corr}}(\mathbf{r}, t) + \mu_i^{\text{hs}}(\mathbf{r}, t). \end{aligned} \quad (5)$$

The first term of Eq. (5) is the ideal-gas chemical potential; the thermal wavelength Λ_i of species i that appears here is irrelevant as it drops upon calculating the flux densities $j_i(x, t)$. The second term of Eq. (5) is the mean-field electrostatic energy; this term results from a Coulomb functional that treats electrostatic interactions at the mean-field level. Inserting the first two terms of Eq. (5) into Eq. (4a), one finds a flux density due to diffusion and electromigration: $j_i = -D(\partial_x \rho_i + z_i \rho_i \partial_x \phi)$, which for $i = \{+, -\}$ corresponds to the Nernst–Planck equation.

Next, the hard-wall electrode surfaces give rise to the following external potential:

$$\frac{V^{\text{ext}}(\mathbf{r})}{k_B T} = \begin{cases} \infty & (x < \sigma/2) \text{ or } (x > L - \sigma/2), \\ 0 & (\text{otherwise}). \end{cases} \quad (6)$$

For dense electrolytes and ionic liquids, dispersion interactions, electrostatic correlations, and steric repulsions cannot be ignored.^{24,30,32,41} We account for dispersion interactions through the pairwise additive Lennard-Jones (LJ) potential treated at the mean-field level. Specifically, for a particle of species $i = \{+, -, 0\}$

at position \mathbf{r} that interacts with a particle of species j at position \mathbf{r}_j , $\mu_i^{LJ}(\mathbf{r}, t)$ is given by the summation of the same LJ potential between all particles as shown in the following equation:

$$\mu_i^{LJ}(\mathbf{r}, t) = \sum_{j=\{+, -, 0\}} \int_{|\mathbf{r}-\mathbf{r}_j|>\sigma} \rho_j(\mathbf{r}_j) \phi^{LJ}(|\mathbf{r}-\mathbf{r}_j|) d\mathbf{r}_j, \quad (7)$$

where ϕ^{LJ} is the pairwise additive LJ potential,

$$\phi^{LJ}(r) = 4\epsilon_{LJ} \left[\left(\frac{\sigma}{r} \right)^{12} - \left(\frac{\sigma}{r} \right)^6 \right]. \quad (8)$$

To improve on our mean-field treatment of electrostatic interactions, we account for electrostatic correlations through the mean spherical approximation.^{30,32,42–44} Their contribution $\mu_i^{\text{corr}}(\mathbf{r}, t)$ to the chemical potential of ions, $i = \{+, -\}$, is expressed as the electrostatic excess correlation of species i , in a reference system at the average concentration ρ_s ,

$$\mu_i^{\text{corr}}(\mathbf{r}, t) = k_B T \sum_{j=\{+, -\}} \int [\rho_j(\mathbf{r}') - \rho_s] c_{ij}^{\text{corr}}(|\mathbf{r}-\mathbf{r}'|) d\mathbf{r}', \quad (9)$$

where $c_{ij}^{\text{corr}}(\mathbf{r})$ is the non-mean-field part of the direct correlation function for ions of species i and j . $c_{ij}^{\text{corr}}(\mathbf{r})$ is the direct correlation function of a reference fluid, which is similar to a bulk reservoir at the same average concentration for ions. For $c_{ij}^{\text{corr}}(|\mathbf{r}|)$, we use the mean spherical approximation, details of which are in Ref. 30.

Finally, we use the modified fundamental measure theory⁴⁵ (see also Ref. 46) to model the steric interactions among particles as hard-sphere interactions. These interactions contribute to Eq. (5) as

$$\mu_i^{\text{hs}}(\mathbf{r}, t) = k_B T \sum_{\alpha} \int \xi_{\alpha}(\mathbf{r}') \omega_i^{\alpha}(|\mathbf{r}'-\mathbf{r}|) d\mathbf{r}', \quad (10)$$

in which $\alpha = \{0, 1, 2, 3, V1, V2\}$ and where

$$\begin{aligned} \xi_0(\mathbf{r}) &= -\ln[1 - n_3(\mathbf{r})], \\ \xi_1(\mathbf{r}) &= -\frac{n_2(\mathbf{r})}{1 - n_3(\mathbf{r})}, \\ \xi_2(\mathbf{r}) &= \left(\frac{\ln[1 - n_3(\mathbf{r})]}{n_3(\mathbf{r})} + \frac{1}{1 - n_3^2(\mathbf{r})} \right) \frac{n_2^2(\mathbf{r}) - \mathbf{n}_{V2}^2(\mathbf{r})}{12\pi n_3(\mathbf{r})} - \frac{n_1(\mathbf{r})}{1 - n_3(\mathbf{r})}, \\ \xi_3(\mathbf{r}) &= \left(\frac{\ln(1 - n_3(\mathbf{r}))}{18\pi n_3^3(\mathbf{r})} + \frac{1 - 3n_3(\mathbf{r}) + [1 - n_3(\mathbf{r})]^2}{36\pi n_3^2(\mathbf{r}) [1 - n_3(\mathbf{r})]^3} \right) \\ &\quad \times (3n_2(\mathbf{r}) \mathbf{n}_{V2}^2(\mathbf{r}) - n_3^3(\mathbf{r})) \\ &\quad + \frac{n_0(\mathbf{r})}{1 - n_3(\mathbf{r})} + \frac{n_1(\mathbf{r}) n_2(\mathbf{r}) - \mathbf{n}_{V1}(\mathbf{r}) \cdot \mathbf{n}_{V2}(\mathbf{r})}{[1 - n_3(\mathbf{r})]^2}, \\ \xi_{V1}(\mathbf{r}) &= -\frac{\mathbf{n}_{V2}(\mathbf{r})}{1 - n_3(\mathbf{r})}, \\ \xi_{V2}(\mathbf{r}) &= -\left(\frac{\ln[1 - n_3(\mathbf{r})]}{n_3(\mathbf{r})} + \frac{1}{1 - n_3^2(\mathbf{r})} \right) \frac{n_2(\mathbf{r}) \mathbf{n}_{V2}(\mathbf{r})}{6\pi n_3^2(\mathbf{r})} - \frac{\mathbf{n}_{V1}(\mathbf{r})}{1 - n_3(\mathbf{r})}. \end{aligned} \quad (11)$$

Here, $n_{\alpha}(\mathbf{r})$ are weighted densities defined as

$$n_{\alpha}(\mathbf{r}) = \sum_i n_{\alpha,i}(\mathbf{r}) = \sum_i \int \rho_i(\mathbf{r}') \omega_i^{\alpha}(|\mathbf{r}'-\mathbf{r}|) d\mathbf{r}'. \quad (12)$$

The weight functions ω_i^{α} of Eq. (12) are provided in Ref. 45. Different from the scalar weight functions ω_i^{α} with $\alpha = \{0, 1, 2, 3\}$, ω_i^{V2} is a surface vector weight function related to the variance across the surface,

$$\omega_i^{V2}(\mathbf{r}) = \frac{\mathbf{r}}{r} \delta(r - \sigma/2), \quad (13)$$

where $\delta(r)$ is the Dirac delta function. Finally, $\omega_i^{V1}(\mathbf{r})$ is given by

$$\omega_i^{V1}(\mathbf{r}) = \frac{\omega_i^{V2}(\mathbf{r})}{2\pi\sigma}. \quad (14)$$

C. Implementation

The boundary conditions Eq. (1a) guarantee a fixed number of particles in our setup, which corresponds to the NVT canonical ensemble in the realization of DDFT. This implies that we specify ρ_s and ρ_{sol} as defined in Eq. (2) and calculate the chemical potential [Eq. (5)] rather than fixing the chemical potentials and calculate the densities, as is common in equilibrium DFT.

We first carried out classical density functional calculations in the NVT ensemble at 0 V. These yielded inhomogeneous equilibrium densities, which then served as the initial condition for our DDFT calculations for finite V_0 . This voltage difference is shared equally by both electrodes, as the model cations and anions are identical except for their charge. At $t = 0$, we thus set the voltages of the two electrodes to $V_0/2$ and $-V_0/2$, respectively. In our implementation of the DDFT (see also Refs. 30 and 32), the ionic density profiles are discretized through differential time frames. For a time step from t_k to $t_{k+1} = t_k + \delta t$, the equation of continuity Eq. (3b) is expressed as an ordinary differential equation. We use an initial guess from the fourth-order Adams–Bashforth (AB) predictor for faster convergence of our Picard iterations. We evaluate the densities $\rho_i(\mathbf{r}, t_{k+1})$ at time step $k + 1$ (for $k \geq 2$) using the fourth-order Adams–Moulton (AM) algorithm,

$$\begin{aligned} \rho_i(\mathbf{r}, t_{k+1}) &= \rho_i(\mathbf{r}, t_k) + \frac{\delta t}{24} (9M_i[\{\rho_i(\mathbf{r}, t_{k+1})\}, t_{k+1}] \\ &\quad + 19M_i[\{\rho_i(\mathbf{r}, t_k)\}, t_k] - 5M_i[\{\rho_i(\mathbf{r}, t_{k-1})\}, t_{k-1}] \\ &\quad + M_i[\{\rho_i(\mathbf{r}, t_{k-2})\}, t_{k-2}]), \end{aligned} \quad (15)$$

where $M_i[\{\rho_i(\mathbf{r}, t)\}, t]$ is the divergence of flux density. The first two time frames ($k = 0$ and 1) of the DDFT calculation, for the start of the charging process, follow from

$$\begin{aligned} \rho_i(\mathbf{r}, t_{k+1}) &= \rho_i(\mathbf{r}, t_k) + \frac{\delta t}{2} (M_i[\{\rho_i(\mathbf{r}, t_{k+1})\}, t_{k+1}] \\ &\quad + M_i[\{\rho_i(\mathbf{r}, t_k)\}, t_k]), \end{aligned} \quad (16)$$

in which the initial densities $\rho_i(\mathbf{r}, t_0)$ are obtained from the equilibrium density distributions at 0 V. Both ionic and solvent densities are rescaled at every iteration step to conserve the average densities.

D. Parameter settings

We use the same LJ potential for the interactions between all three species, with a well depth $\epsilon_{LJ} = 0.7k_B T$ and interaction range set by the particle diameters σ . Unless stated otherwise, we use $\sigma = 0.5$ nm, which is typical for ionic liquid molecules.⁴⁷ We vary ρ_s between 0.05 and 3.5 M while keeping the total average concentration $\rho_{\text{tot}} = 2\rho_s + \rho_{\text{sol}}$ fixed to $\rho_{\text{tot}} = 0.527\sigma^{-3} = 7.0$ M through compensating changes in ρ_{sol} . Both ρ_s and ρ_{sol} are varied. Hence, with the constraint that the total density is fixed, to study the dependence on salt concentrations for charging dynamics. We set the temperature to $T = 298$ K and the plate separation to $L = 12\sigma$ and use a fixed relative permittivity $\epsilon_r = 2$ and diffusion coefficient $D = 4.3 \times 10^{-11} \text{ m}^2 \text{ s}^{-1}$. By doing so, we ignore the salt-concentration dependence of ϵ and D ,³³ which we leave for scrutiny in future work. Unless otherwise stated, we considered $V_0 = 1$ V. In our time integration scheme, we use a fixed time step $\delta t = 5 \times 10^{-4} \tau_\sigma$, with $\tau_\sigma = \sigma^2/D$ being the typical time for an ion to diffuse over its diameter.

III. RESULTS

A. Density profiles

In Fig. 2(a), we plot the local particle concentration relative to its average value, $|\rho_{\text{tot}} - \sum_i \rho_i(x, t)|\sigma^3$, during charging at $\rho_s = 2.0$ M. From the data collapse in this panel for $0 < x < 3\sigma$, we see that this observable does not vary much with time. By contrast, for the same ρ_s , Fig. 2(b) shows that the ionic charge density develops strong oscillations that signal the formation of increasingly pronounced alternating layers of cations and anions. Interestingly, the slope of the envelope of Fig. 2(b) decreases with time, which means that the decay length of the charging profile increases with time. Figure 2(c) shows the local charge density (solid lines) and solvent density (dashed lines) at the late time $t = 10\tau_\sigma$ for several ρ_s . As is clear from the inset of Fig. 2(c), ions form more pronounced layers for larger ρ_s .

B. Charge and salt density relaxation

With the ionic density profiles at hand, we determine $\phi(x, t)$ by Eq. (3a) and the electrode surface charge density by Gauss's law,

$$Q(t) = -\frac{\epsilon_0 \epsilon_r k_B T}{e} \partial_x \phi(x=0, t). \quad (17)$$

Figure 3(a) shows $Q(t)$ in units of e/σ^2 for several ρ_s . As our system relaxes slower for more dilute electrolytes, we determined $Q(t)$ up to $t = 20\tau_\sigma$ for 3.5 M and up to $t = 300\tau_\sigma$ for 0.05 M. We denote the electrode charge at the end of these charging processes by Q_{eq} ; in Fig. 3(a), we see that Q_{eq} increases with ρ_s and then saturates.

Figure 3(b) shows that the scaled electrode charge $1 - Q(t)/Q_{\text{eq}}$ (solid lines) relaxes biexponentially, which is consistent with previous studies.^{19,20,23,24,48} The same panel also shows the normalized concentration $(c(t) - c_{\text{eq}})/(c(0) - c_{\text{eq}})$ (dashed lines), with $c(t)$ being the total particle concentration in the middle of the slit,

$$c(t) = \sum_{i \in \{+, -, 0\}} \rho_i(x=L/2, t) \quad (18)$$

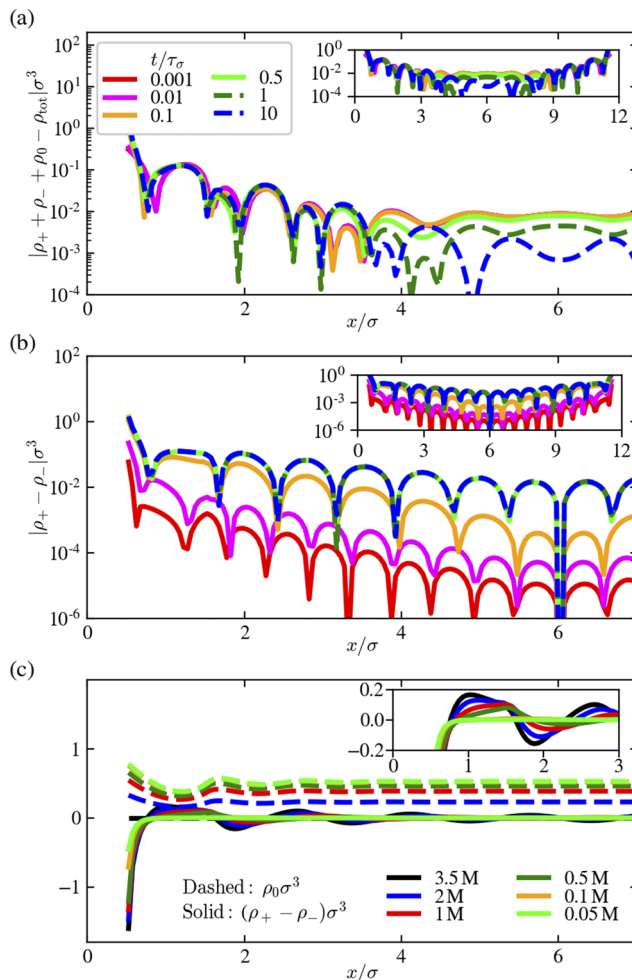


FIG. 2. Profiles of (a) the deviation of the total concentration from its average value and (b) the charge density at several times t after switching on a potential difference of 1 V between the two planar electrodes separated by a distance $L = 12\sigma$ at a salt concentration $\rho_s = 2.0$ M. The main panels show the region near one electrode surface; the insets present the same profiles across the whole system. (c) The local solvent density (dashed lines) and charge density (solid lines) for several ρ_s at the late time $t = 10\tau_\sigma$. Charge densities $\rho_+ - \rho_-$ are further presented in the inset.

and $c(0)$ and c_{eq} being the initial and final values of $c(t)$. At late times, the ionic concentration and ionic charge in Fig. 3(b) decay with similar slopes; hence, they then have similar relaxation times.

Next, Fig. 3(c) shows the scaled charge density $1 - Q(t)/Q_{\text{eq}}$ for several V_0 . This panel shows that the scaled charge density relaxes biexponentially, with slower relaxation at late times. This late-time slow-down sets in earlier and more prominently for larger V_0 . Note that the early-time data in Fig. 3(c) collapses over a wide range of V_0 : this is in contrast to a previous DDFT study³⁰ that found V_0 -dependent early-time relaxation. We return to this discrepancy in Sec. IV. As we show below, our findings are in line with solutions to the Poisson–Nernst–Planck (PNP) equations, both linearized²² and into the nonlinear regime.¹⁹

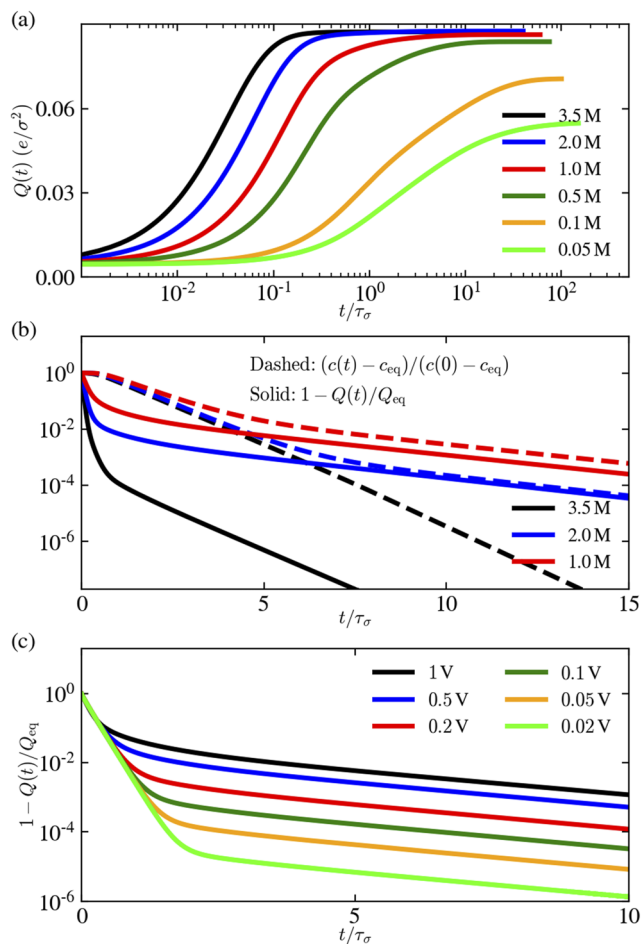


FIG. 3. (a) The areal electrode charge $Q(t)$ as a function of time t after the voltage switch to $V_0 = 1$ V for several average ion concentrations ρ_s . (b) The scaled electrode charge density (solid lines) and the total concentration at the middle of the slit (dashed lines) for $\rho_s = 1.0, 2.0,$ and 3.5 M. (c) The scaled electrode charge density for $\rho_s = 1.0$ M and applied voltages between $V_0 = 0.02$ and 1 V.

C. Relaxation timescales

To characterize the biexponential decay of $Q(t)$, we introduce the instantaneous relaxation time

$$\tau(t) = - \left[\frac{d \ln(1 - Q(t)/Q_{eq})}{dt} \right]^{-1} \quad (19)$$

shown in Fig. 4(a) for the parameters of Fig. 3(b). Notably, $\tau(t)$ transitions between early- and late-time plateaus whose heights are denoted by τ_1 and τ_2 , respectively. We see that τ_1 decreases with increasing ρ_s and that τ_2 is similar for $\rho_s = 1.0$ M and $\rho_s = 2.0$ M, consistent with the observed similar slopes for $1 - Q(t)/Q_{eq}$ in Fig. 3(b).

The relaxation time τ_1 is explained well by a simple equivalent circuit. The capacitance of each of the two electric double layers (EDLs) in our system can be approximated by a series connection of two Helmholtz capacitors, one of width λ_D for the diffuse part

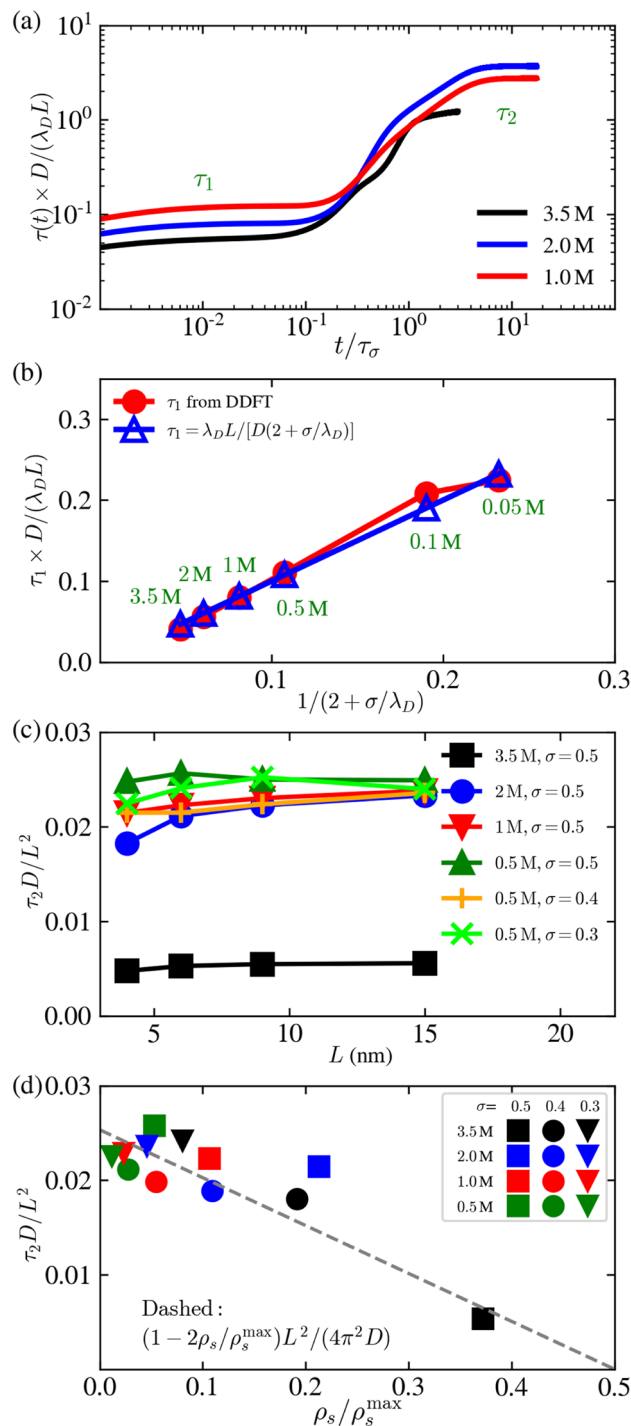


FIG. 4. (a) Instantaneous relaxation time function $\tau(t)$ normalized by $\lambda_D L / (2D)$. (b) The initial relaxation time τ_1 scaled by $D/(\lambda_D L)$ vs $1/(2 + \sigma/\lambda_D)$ from DDFT (red circles) and analytical theory (blue triangles) for salt concentrations between 0.05 and 3.5 M. (c) The late-time relaxation time $\tau_2 D/L^2$ vs L for various ρ_s and σ . (d) $\tau_2 D/L^2$ vs ρ_s^{\max} for various σ as indicated in units of nm, with $L = 15$ nm; the dashed line represents the analytical prediction from Ref. 20, corrected with a factor π^2 from Ref. 48.

of the EDL and one of width λ_S for the charge-free Stern layer next to the electrode. In our case, the ions of diameter σ lead to a Stern layer of width $\lambda_S = \sigma/2$ [cf. Fig. 2(b)]. Multiplying the electrolyte's areal resistance $R = \lambda_D^2 L / (\epsilon_0 \epsilon_r D)$ by the total areal capacitance $C = \epsilon_0 \epsilon_r / [2(\lambda_D + \lambda_S)]$ then yields $RC = \lambda_D L / [2D(1 + \lambda_S/\lambda_D)]$ —the same expression follows from the linearized PNP equations.^{19,21,22}

Figure 4(b) shows τ_1 (red circles) scaled by $D/(\lambda_D L)$ vs $1/(2 + \sigma/\lambda_D)$ for different ρ_s . With this scaling and axes, the RC timescale (blue triangles) falls on the diagonal. As we used Helmholtz's simple expression for the EDL capacitance, the above equivalent circuit can only be expected to describe our model's relaxation for applied potentials smaller than the thermal voltage (≈ 26 mV). Surprisingly, however, even at voltages as high as $V_0 = 1$ V as applied here, the DDFT data collapse onto the blue diagonal. To our knowledge, this constitutes the first numerical evidence that the EDL capacitors with finite-size ions relax with the RC time $\lambda_D L / [2D(1 + \lambda_S/\lambda_D)]$ of Refs. 19, 21, and 22. Note how Fig. 4(a) underlines the importance of the τ_1 timescale: τ_1 describes the relaxation of $Q(t)$ up to $t/\tau_\sigma \approx 0.1$, by which time $Q(t)$ has almost reached its final value, $Q(0.1\tau_\sigma) \approx 0.8Q_{\text{eq}}$.

The larger late-time relaxation time τ_2 is caused by the adsorption of salt in the EDL: a dip in the salt concentration near the EDL at early times is filled by salt fluxes on the diffusion time.¹⁹ Figure 4(c) shows $\tau_2 D/L^2$ vs L for $\rho_s = 0.5, 1.0, 2.0,$ and 3.5 M. These curves being flat confirms the diffusive scaling $\tau_2 \propto L^2/D$. Kilic and co-workers proposed a modified PNP model, for which they found $\tau_2 = (1 - 2\rho_s/\rho_s^{\text{max}})L^2/(4D)$.²⁰ The maximal concentration $\rho_s^{\text{max}} = \eta/(2 \times 1/6\pi\sigma^3)$ amounts for our setup to $\rho_s^{\text{max}} = 1/(\sqrt{2}\sigma^3)$, where we used the density of hexagonal close packing $\eta = \pi/(3\sqrt{2})$. Figure 4(d) shows numerical $\tau_2 D/L^2$ data (symbols) and the theoretical prediction $(1 - 2\rho_s/\rho_s^{\text{max}})/(4\pi^2)$ (dashed line), both vs $\rho_s/\rho_s^{\text{max}}$. Note that we added a factor $\pi^2 \approx 10$ after the analytical derivation of Ref. 48. With this factor included, we observe good agreement between the numerical data and analytical prediction.

IV. DISCUSSION

We found in Fig. 3(c) that $1 - Q(t)/Q_{\text{eq}}$ for different applied potentials V_0 collapse on a single curve at early times; hence, the timescale τ_1 of the early-time relaxation does not depend on V_0 . We found the same V_0 -independent early-time charging for other salt concentrations, also when we changed the time step of our DDFT implementation. These findings contrast Fig. 8 of Ref. 30, where charge relaxation did not collapse on a single curve at early times; hence, their relaxation timescale was V_0 -dependent. Yet, as already acknowledged by these authors,⁴⁹ Ref. 30 considered a different measure for the surface charge: instead of the surface charge density $Q(t)$ from Gauss's law [Eq. (17)], they considered the total accumulated ionic charge in half of the system,

$$Q_{\text{ions}}(t) = e \int_0^{L/2} [\rho_+(x, t) - \rho_-(x, t)] dx. \quad (20)$$

Equations (17) and (20) are equivalent if the electric field at the center of the cell vanishes, $\partial_x \phi(x = L/2, t) = 0$.⁴⁹ However, there is no reason to surmise this to be the case in our system, as the electrodes are of opposite polarity. [The energy stored in a capacitor

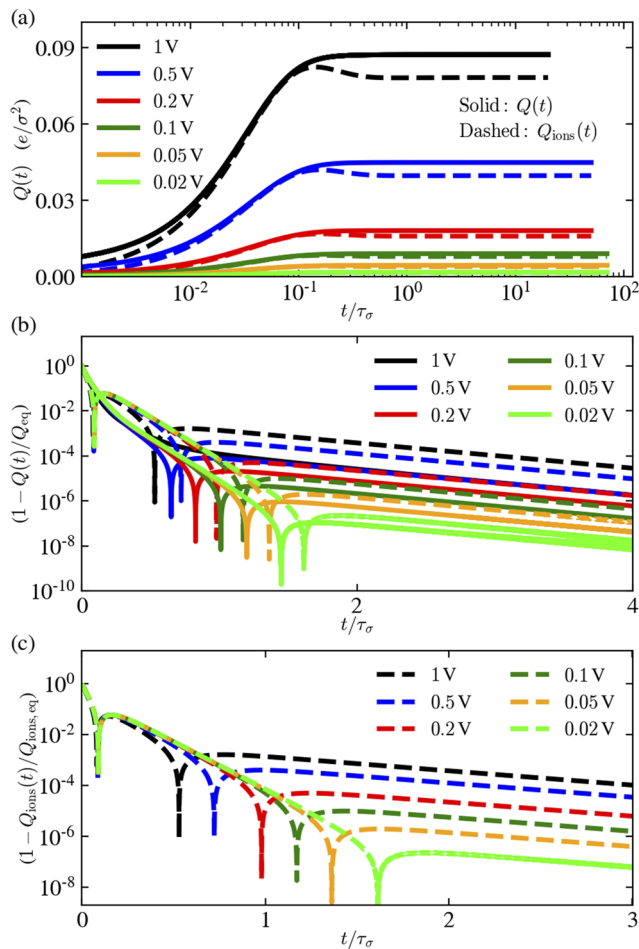


FIG. 5. Panel (a) compares the electrode charge $Q(t)$ (solid) and the accumulated ionic charge $Q_{\text{ions}}(t)$ (dashed) in units of e/σ^2 as a function of time t for $\rho_s = 3.5$ M and electrode voltages between $V_0 = 0.02$ and 1 V. Panel (b) shows the same $Q(t)$ and $Q_{\text{ions}}(t)$ data, scaled to their respective equilibrium values. Panel (c) shows the same $Q_{\text{ions}}(t)$ data in panel (b) but only for up to $t/\tau_\sigma = 3$.

depends on $Q(t)$ rather than on $Q_{\text{ions}}(t)$, making $Q(t)$ more relevant for applications.] As shown in Fig. 5(a), $Q_{\text{ions}}(t)$ (dashed) is systematically lower than $Q(t)$ at various electrode voltages. Next, Figs. 5(b) and 5(c) show the scaled and shifted electrode charge density $[1 - Q(t)/Q_{\text{eq}}]$ and the corresponding scaled total ion accumulation $[1 - Q_{\text{ions}}(t)/Q_{\text{ions,eq}}]$. We observe that, at late times, Q and Q_{ions} relax with the same relaxation time and that Q_{ions} overshoots, while Q does not. Most importantly, at early times, data for the scaled charge and accumulated ion densities collapse for different V_0 . Hence, the difference between Eqs. (17) and (20) does not underlie the V_0 -dependent early-time relaxation found in Ref. 30.

V. CONCLUSION

Using DDFT, we have studied the response of electrolytes between two flat electrodes to a suddenly applied voltage difference

for a wide range of electrolyte concentrations. Near the charged electrodes, we found alternating layers of cationic and anionic charge, in line with density functional theory studies of the equilibrium EDL.^{30,32,41,50} Our work showed how this layered structure builds up on two characteristic timescales, τ_1 and τ_2 . Contrasting a prior DDFT study,³⁰ we find that the early-time relaxation time τ_1 does not depend on the applied voltage: We showed that τ_1 agrees—over a wide range of average concentrations and even for V_0 as large as 1 V—with the RC time $\lambda_D L / [2D(1 + \lambda_S/\lambda_D)]$, which follows from the linearized PNP equations.^{19,21,22} DDFT predictions for the late-time relaxation time τ_2 are decently captured by predictions from the modified PNP theory.²⁰ Hence, even though the PNP and modified PNP theory do not describe ion layering in the EDL,⁴¹ these theories do predict the same timescales of EDL formation as our more accurate DDFT.

SUPPLEMENTARY MATERIAL

The [supplementary material](#) contains three videos to reinforce our findings.

Video 1 presents the transient dimensionless electrostatic potential $\phi(x, t)$ and anionic flux density $j_-(x, t)$ of a slit system with separation $L = 12\sigma$ filled with a pure ionic liquid ($\rho_s = 3.5$ M). We do not show the cationic density flux $j_+(x, t)$ —for which $j_+(L - x, t) = j_-(x, t)$ holds, as cations and anions are modeled as equal-sized, oppositely charged spheres. $j_-(x, t) > 0$ shortly after applying the voltage difference, which means that anions move uniformly toward the electrode at $x = 0$ (from right to left). Around $t > 0.1\tau_\sigma$, $j_-(x, t)$ oscillates across the whole slit with a wavelength close to the ion size σ . For these times, the EDL rearranges into cation-rich and anion-rich layers. From $t = 1.0\tau_\sigma$ onward, $j_-(x, t)$ is directed to both electrodes, changing sign in the middle of the slit. From [Fig. 4\(a\)](#) of the main text, we see that these times correspond to the diffusive τ_2 relaxation.

Video 2 is identical to Video 1, except for a larger electrode separation of $L = 24\sigma$. Oscillations in $j_-(x, t)$ appear in Video 2 later ($t = 0.15\tau_\sigma$) than in Video 1 ($t = 0.1\tau_\sigma$). From comparing the time at which the potential $\phi(x = \sigma/2, t)$ drops below zero in Video 2 ($t = 0.1\tau_\sigma$) and in Video 1 ($t = 0.035\tau_\sigma$), we again see that the EDL develops slower for larger electrode separation.

Video 3 is identical to Video 1, except for a smaller salt concentration $\rho_s = 1$ M. Comparing Videos 1 and 3, we see that the EDLs develop faster for smaller salt concentration, in line with [Fig. 4\(a\)](#) of the main text. In the video, we also present the solvent density flux $j_0(x, t)$. We see that $j_0(x, t)$ oscillates at early times with a period comparable to the particle size. Around $t = 0.1\tau_\sigma$, the period of these oscillations starts to increase, until $t = 2.5\tau_\sigma$, when $j_0(x, t)$ is uniformly directed toward the center $x = L/2$ of the slit, hence opposite to the anionic flux density.

ACKNOWLEDGMENTS

This work was supported by the National Natural Science Foundation of China (Grant Nos. 21703153, 21808055, and 22078088). This work was completed, in part, with the resources provided by the School of Materials Science and Engineering, Tianjin University of Technology, China. This work was part of the

D-ITP consortium, a program of the Netherlands Organization for Scientific Research (NWO) that is funded by the Dutch Ministry of Education, Culture and Science (OCW). The research leading to these results has received funding from the European Union's Horizon 2020 Research and Innovation Programme under the Marie Skłodowska-Curie Grant Agreement No. 801133. We acknowledge the EU-FET project NANOPHLOW (Grant No. REP-766972-1) and helpful discussions with Timur Aslyamov, Willem Boon, Andreas Härtel, Honglai Liu, and Christian Pedersen.

AUTHOR DECLARATIONS

Conflict of Interest

The authors have no conflicts to disclose.

Author Contributions

K.M. and M.J. contributed equally to this work.

DATA AVAILABILITY

The data that support the findings of this study are available from the corresponding author upon reasonable request.

REFERENCES

- 1 J. P. Keener and J. Sneyd, *Mathematical Physiology* (Springer, 1998), Vol. 1.
- 2 W. J. Nicolas, M. S. Grison, S. Trépout, A. Gaston, M. Fouché, F. P. Cordelières, K. Oparka, J. Tilsner, L. Brocard, and E. M. Bayer, *Nat. Plants* **3**, 17082 (2017).
- 3 M. E. Suss, S. Porada, X. Sun, P. M. Biesheuvel, J. Yoon, and V. Presser, *Energy Environ. Sci.* **8**, 2296 (2015).
- 4 C. Zhan, C. Lian, Y. Zhang, M. W. Thompson, Y. Xie, J. Wu, P. R. C. Kent, P. T. Cummings, D. e. Jiang, and D. J. Wesolowski, *Adv. Sci.* **4**, 1700059 (2017).
- 5 Y. He, R. Qiao, J. Vatamanu, O. Borodin, D. Bedrov, J. Huang, and B. G. Sumpter, *J. Phys. Chem. Lett.* **7**, 36 (2016).
- 6 Z. Bo, C. Li, H. Yang, K. Ostrikov, J. Yan, and K. Cen, *Nano-Micro Lett.* **10**, 33 (2018).
- 7 K. Breitsprecher, C. Holm, and S. Kondrat, *ACS Nano* **12**, 9733 (2018).
- 8 Y. M. Liu, C. Merlet, and B. Smit, *ACS Cent. Sci.* **5**, 1813 (2019).
- 9 S. Bi, H. Banda, M. Chen, L. Niu, M. Chen, T. Wu, J. Wang, R. Wang, J. Feng, T. Chen *et al.*, *Nat. Mater.* **19**, 552 (2020).
- 10 X. Wang, A. Y. Mehandzhyski, B. Arstad, K. L. Van Aken, T. S. Mathis, A. Gallegos, Z. Tian, D. Ren, E. Sheridan, B. A. Grimes *et al.*, *J. Am. Chem. Soc.* **139**, 18681 (2017).
- 11 A. C. Forse, C. Merlet, J. M. Griffin, and C. P. Grey, *J. Am. Chem. Soc.* **138**, 5731 (2016).
- 12 Q. Dou, L. Liu, B. Yang, J. Lang, and X. Yan, *Nat. Commun.* **8**, 2188 (2017).
- 13 J. Chmiola, G. Yushin, Y. Gogotsi, C. Portet, P. Simon, and P. L. Taberna, *Science* **313**, 1760 (2006).
- 14 M. A. Gebbie, M. Valtiner, X. Banquy, E. T. Fox, W. A. Henderson, and J. N. Israelachvili, *Proc. Natl. Acad. Sci. U. S. A.* **110**, 9674 (2013).
- 15 A. M. Smith, A. A. Lee, and S. Perkin, *J. Phys. Chem. Lett.* **7**, 2157 (2016).
- 16 R. Tivony, S. Safran, P. Pincus, G. Silbert, and J. Klein, *Nat. Commun.* **9**, 4203 (2018).
- 17 C. S. Perez-Martinez and S. Perkin, *Soft Matter* **15**, 4255 (2019).
- 18 L. Richter, P. J. Żuk, P. Szymczak, J. Paczesny, K. M. Bąk, T. Szyborski, P. Garstecki, H. A. Stone, R. Hołyst, and C. Drummond, *Phys. Rev. Lett.* **125**, 056001 (2020).
- 19 M. Z. Bazant, K. Thornton, and A. Ajdari, *Phys. Rev. E* **70**, 021506 (2004).
- 20 M. S. Kilic, M. Z. Bazant, and A. Ajdari, *Phys. Rev. E* **75**, 021503 (2007).
- 21 F. Beunis, F. Strubbe, M. Marescaux, K. Neyts, and A. R. M. Verschueren, *Appl. Phys. Lett.* **91**, 182911 (2007).

- ²²M. Janssen and M. Bier, *Phys. Rev. E* **97**, 052616 (2018).
- ²³B. Balu and A. S. Khair, *Soft Matter* **14**, 8267 (2018).
- ²⁴C. Lian, M. Janssen, H. Liu, and R. van Roij, *Phys. Rev. Lett.* **124**, 076001 (2020).
- ²⁵X. Jiang, J. Huang, H. Zhao, B. G. Sumpter, and R. Qiao, *J. Phys.: Condens. Matter* **26**, 284109 (2014).
- ²⁶A. A. Lee, S. Kondrat, D. Vella, and A. Goriely, *Phys. Rev. Lett.* **115**, 106101 (2015).
- ²⁷A. J. Asta, I. Palaia, E. Trizac, M. Levesque, and B. Rotenberg, *J. Chem. Phys.* **151**, 114104 (2019).
- ²⁸C. Noh and Y. Jung, *Phys. Chem. Chem. Phys.* **21**, 6790 (2019).
- ²⁹M. Ma, Z. Xu, and L. Zhang, *SIAM J. Appl. Math.* **81**, 1645 (2021).
- ³⁰J. Jiang, D. Cao, D.-e. Jiang, and J. Wu, *J. Phys.: Condens. Matter* **26**, 284102 (2014).
- ³¹J. Jiang, D. Cao, D.-e. Jiang, and J. Wu, *J. Phys. Chem. Lett.* **5**, 2195 (2014).
- ³²C. Lian, S. Zhao, H. Liu, and J. Wu, *J. Chem. Phys.* **145**, 204707 (2016).
- ³³H. Gao, Y. Chang, and C. Xiao, *Chem. Lett.* **46**, 1258 (2017).
- ³⁴H. Gao and C. Xiao, *Europhys. Lett.* **124**, 58002 (2018).
- ³⁵S. Babel, M. Eikerling, and H. Löwen, *J. Phys. Chem. C* **122**, 21724 (2018).
- ³⁶L. Qing, Y. Li, W. Tang, D. Zhang, Y. Han, and S. Zhao, *Langmuir* **35**, 4254 (2019).
- ³⁷L. Qing, J. Lei, T. Zhao, G. Qiu, M. Ma, Z. Xu, and S. Zhao, *Langmuir* **36**, 4055 (2020).
- ³⁸W. Tang, H. Yu, T. Zhao, L. Qing, X. Xu, and S. Zhao, *Chem. Eng. Sci.* **236**, 116513 (2021).
- ³⁹M. te Vrugt, H. Löwen, and R. Wittkowski, *Adv. Phys.* **69**, 121 (2020).
- ⁴⁰M. Schmidt, “Power functional theory for many-body dynamics,” *Rev. Mod. Phys.* (to be published) (2022); arXiv:2111.00432; available at <https://journals.aps.org/rmp/accepted/39079E1cT971450d207f6c58e99bfe964bc742adc>.
- ⁴¹A. Härtel, M. Janssen, S. Samin, and R. van Roij, *J. Phys.: Condens. Matter* **27**, 194129 (2015).
- ⁴²L. Blum and J. S. Høye, *J. Phys. Chem.* **81**, 1311 (1977).
- ⁴³D. Henderson and L. Blum, *J. Chem. Phys.* **69**, 5441 (1978).
- ⁴⁴P. Cats, R. Evans, A. Härtel, and R. van Roij, *J. Chem. Phys.* **154**, 124504 (2021).
- ⁴⁵Y.-X. Yu and J. Wu, *J. Chem. Phys.* **117**, 10156 (2002).
- ⁴⁶R. Roth, R. Evans, A. Lang, and G. Kahl, *J. Phys.: Condens. Matter* **14**, 12063 (2002).
- ⁴⁷C. Largeot, C. Portet, J. Chmiola, P.-L. Taberna, Y. Gogotsi, and P. Simon, *J. Am. Chem. Soc.* **130**, 2730 (2008).
- ⁴⁸I. Palaia, “Charged systems in, out of, and driven to equilibrium: From nanocapacitors to cement,” Ph.D. thesis, Université Paris-Saclay, 2019, pp. 26–28.
- ⁴⁹J. Jiang, D. Cao, D.-e. Jiang, and J. Wu, *J. Phys. Chem. Lett.* **11**, 10203 (2020).
- ⁵⁰P. Cats and R. van Roij, *J. Chem. Phys.* **155**, 104702 (2021).